# Supplementary Material for 'Significantly increased extreme precipitation expected in Europe and North America from extratropical cyclones'

Matt Hawcroft*, Ella Walsh, Kevin Hodges & Giuseppe Zappa

* Correspondence to: Matt Hawcroft (m.hawcroft@exeter.ac.uk)

## Section 1. Precipitation around composite cyclones

Statistical analysis of cyclone precipitation intensity uses the mean precipitation within a 5° radial cap of the cyclone centre. Previous work has shown results to be relatively insensitive to the exact cap used for such analysis*(4,18,30)*, since most precipitation falls within the inner 5°. The analysis in the main text uses precipitation at all stages in the lifecycle of the composite cyclones in Figure 1 and at the time of maximum precipitation elsewhere. The analysis in Figures 2-3 has been repeated using mean along track precipitation from the 48-hours up to maximum intensity and the results are qualitatively similar (not shown).

The spatial composites in Supplementary Figure 1 show the distribution of precipitation around the cyclone centre from all storms included in this analysis. They are computed on a 20° radial grid (to capture the majority of the cyclone precipitation, including on fronts) at the time of maximum precipitation intensity, rotated to the direction of propagation of the cyclones. Results have been tested for sensitivity to selecting the time of maximum precipitation for analysis as opposed to the precipitation at maximum vorticity, or a specified offset from maximum vorticity (e.g. -6 hours) and conclusions were insensitive to these changes (not shown).

Supplementary Figure 1 shows ensemble mean composite precipitation from the models for DJF and JJA compared to ERAI, indicating that the models have the ability to produce a spatial distribution of precipitation around cyclones comparable to the reanalysis. The JJA precipitation intensity is slightly weaker than in ERAI, though this may not be a bias (see Supplementary Section 2). Changes from 20$^{th}$ to 21$^{st}$ century are ~18% (see Table 1) and are focused on the region of maximum intensity, where the warm front and maximum ascent occurs*(32,42)*, consistent with these changes being largely thermodynamic (Figure 2(c), Supplementary Text Sections 3 and 4).

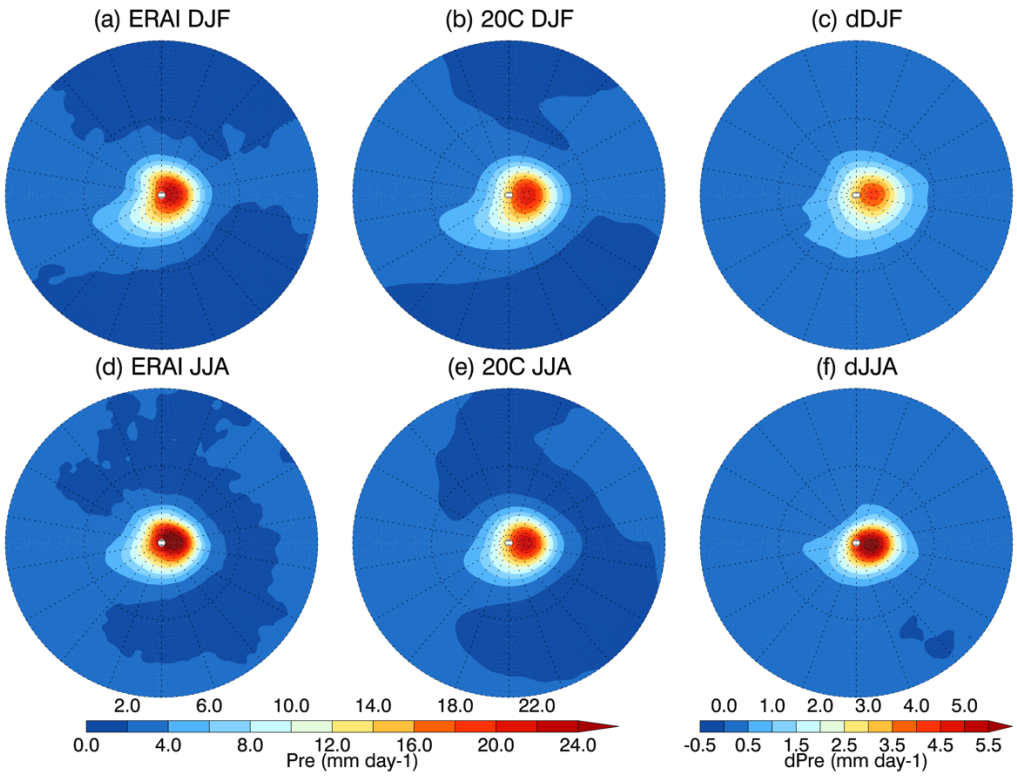


**Supplementary Figure 1.**
Composite precipitation from all cyclones for (a,d) ERAI, (b,e) the 20$^{th}$ century CMIP5 ensemble mean and (c,f) the difference between the 21$^{st}$ and 20$^{th}$ century precipitation in the models (mm day$^{-1}$) in DJF (a-c) and JJA (d-f). Composite radii are 20°. Composites are shown at the time of maximum precipitation intensity.

## Section 2. Cyclone precipitation lifecycles

The models are evaluated against ERAI in the main text. Precipitation data at 6-hourly resolution is available from ERAI allowing detailed analysis throughout composite lifecycles. As noted in the main text and shown in Figure 1, the models' precipitation intensity throughout the composite cyclone lifecycle is comparable to ERAI in DJF but of lower intensity in JJA. In Supplementary Figure 2 we show lifecycles obtained from GPCP for comparison against CMIP5 and ERAI.

GPCP is available at daily resolution, so precipitation data in CMIP5 and ERAI has been degraded to daily resolution, with cyclone locations identified at 12UTC for compositing, using data and following the procedures outlined in previous work (*30*). In DJF, GPCP

and ERAI compare closely and the models produce precipitation intensities that compare favourably to both datasets, further enhancing confidence in their ability to represent cyclone associated precipitation. In JJA, there is a clear difference between GPCP and ERAI, with higher precipitation intensities in ERAI. Since neither dataset provides uncertainty estimates, it is difficult to assess bias and the differences between the two may be considered a measure of observational uncertainty, though there are known biases in cloud processes around these storms in ERAI (*33*). Further analysis of the source of the GPCP/ERAI differences are outside the scope of this study, though the model ensemble JJA precipitation can be considered as within observational uncertainty, again providing confidence in the ability of the models to represent cyclone associated precipitation.

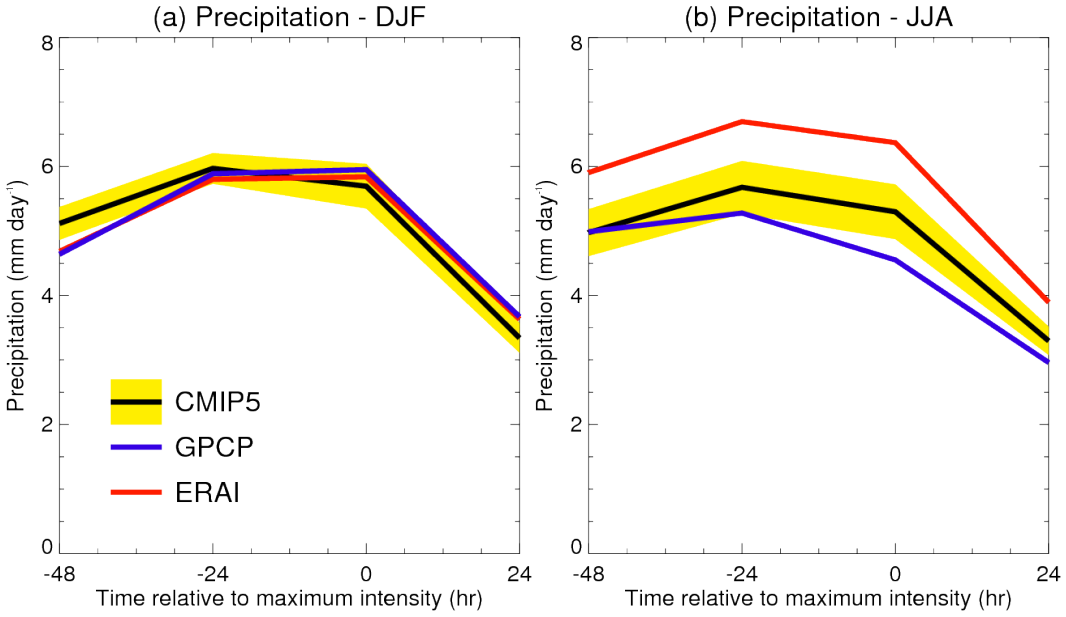


**Supplementary Figure 2**

Composite cyclone precipitation lifecycles for (a) DJF and (b) JJA in CMIP5, ERAI and GPCP. Ensemble mean 20$^{th}$ century precipitation is shown as a solid black line with 95% uncertainty intervals as yellow. Time is shown as hours relative to maximum vorticity. Precipitation is the 24-hourly precipitation accumulation centred on the time the cyclone is identified and averaged within 5° of the cyclone centre.

## Section 3. Dynamical changes in cyclone behaviour

Changes in the precipitation intensity around cyclones may be controlled by changes in atmospheric circulation or by variations in atmospheric moisture content. Figure 2d shows that precipitation scales differentially for weakly and intensely precipitating cyclones when considering the relationship between precipitation and near surface

warming. Supplementary Figure 3(a) and (b) show changes in the dynamical intensity of cyclones. There are few robust changes in the dynamical intensity of cyclones, indicating that the changes in precipitation around cyclones shown in this study are entirely thermodynamic (related to atmospheric moisture content).

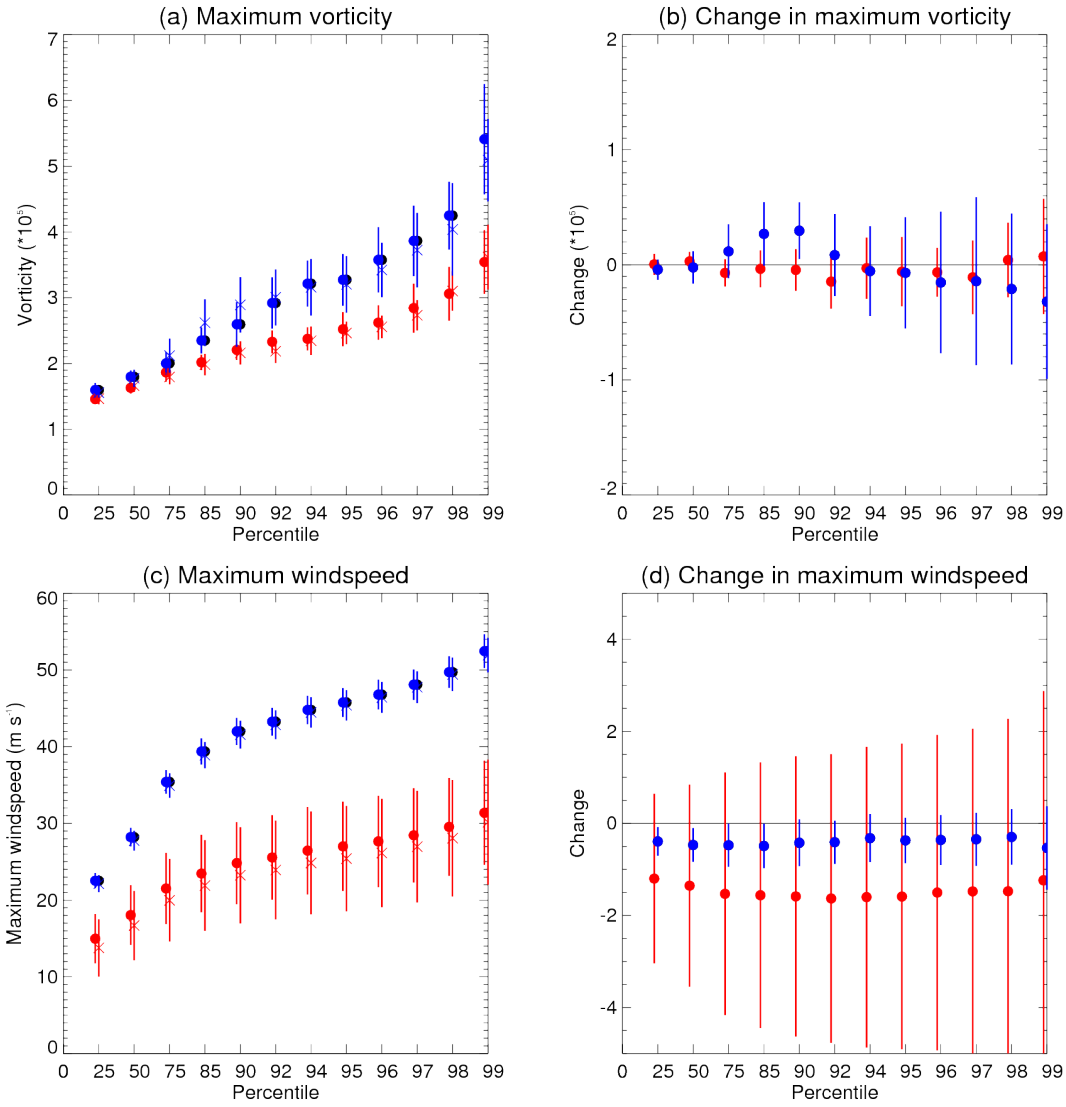


**Supplementary Figure 3**

Dynamical intensity of cyclones in the 20th and 21st century. (a) Maximum relative vorticity at 850hPa ($s^{-1}$) for all Northern Hemisphere storms for DJF (blue) and JJA (red) for 20th (circles) and 21st (crosses) centuries, with 95% uncertainty ranges. Thresholds are intensity percentiles of relative vorticity (from dynamically weak to dynamically intense storms) in each century based on the maximum relative vorticity during each cyclone's lifecycle. (b) Difference from 20th to 21st century. (c) as for (a) but for maximum windspeeds (as defined in the text, m $s^{-1}$), (d) as for (b) but for maximum windspeeds. Note the x-axes are non-linear and the points are slightly offset to aid clarity.

Further, maximum windspeeds (defined here as the strongest 6-hourly sustained windspeed at 850hPa, within 5° of the cyclone centre, in the 48-hours up to maximum dynamical intensity of a cyclone) do not change in the models (Supplementary Figure 3(c) and (d)). Wind gusts cause damage at the surface, though their parameterisation in models is not consistent, making inter-model comparison difficult, so we focus here on the 850hPa level, which is also a relevant level for the dynamical forcing of precipitation. Given our findings of no significant change in either dynamical intensity or wind extremes, to understand future changes in wind gusts and any associated damage, constraining the spatial pattern of the response of the storm tracks to climate warming is key. Changes in wind gusts at individual locations may occur due to changes in cyclone frequency or the behaviour of small scale convective events, even without changes in the dynamics of the synoptic scale systems evaluated here*(18,43,44)*.

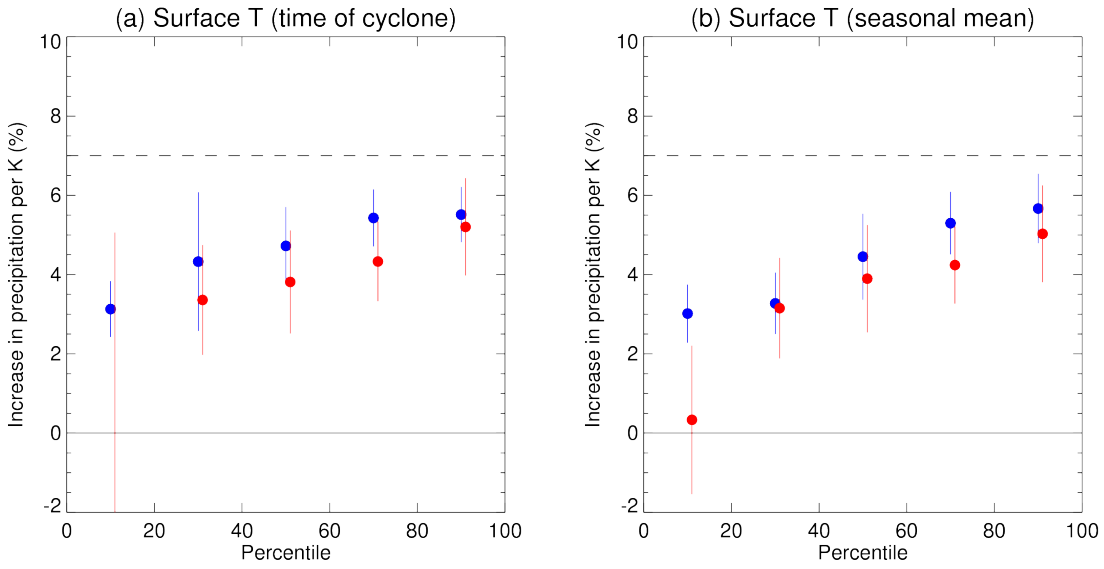


**Supplementary Figure 4**

Changes in precipitation (% $K^{-1}$) scaled by near surface (~2m) air temperature using (a) the temperature at the time of the cyclone's passage (as in Fig 2d) and (b) the seasonal mean temperature at each location for DJF (blue) and JJA (red) with 95% uncertainty ranges. The x-axis percentiles are for maximum precipitation intensities in each analysis period and are split into quintiles as in Fig 2d. Both precipitation and temperature values are the mean within a 5° radial cap of the cyclone centre.

## Section 4. Thermodynamic changes to the environment

As discussed in Supplementary Text Section 2 and the main text, changes in precipitation intensity in cyclones are primarily controlled by changes in atmospheric moisture content. In Figure 2(d) and Supplementary Figure 4(a) the maximum precipitation in cyclones is shown to scale from ~3% $K^{-1}$ for weaker cyclones (excluding the weakest summer cyclones which produce very little precipitation) to ~6% $K^{-1}$ for more intensely precipitating cyclones.

In this analysis, the surface temperature data is taken from a 5° radial cap around the cyclone at the time of each cyclone's passage. Frequently, analyses of changes in precipitation are undertaken in the context of changes in (seasonal) mean surface temperature. In Supplementary Figure 4(b) we show the same analysis but with seasonal mean surface temperature used rather than the instantaneous temperature at the time of each storm. The results are qualitatively similar indicating that the thermodynamic controls on precipitation are associated with large-scale, seasonal mean patterns of surface temperature change rather than local changes related to the environment of individual cyclones.

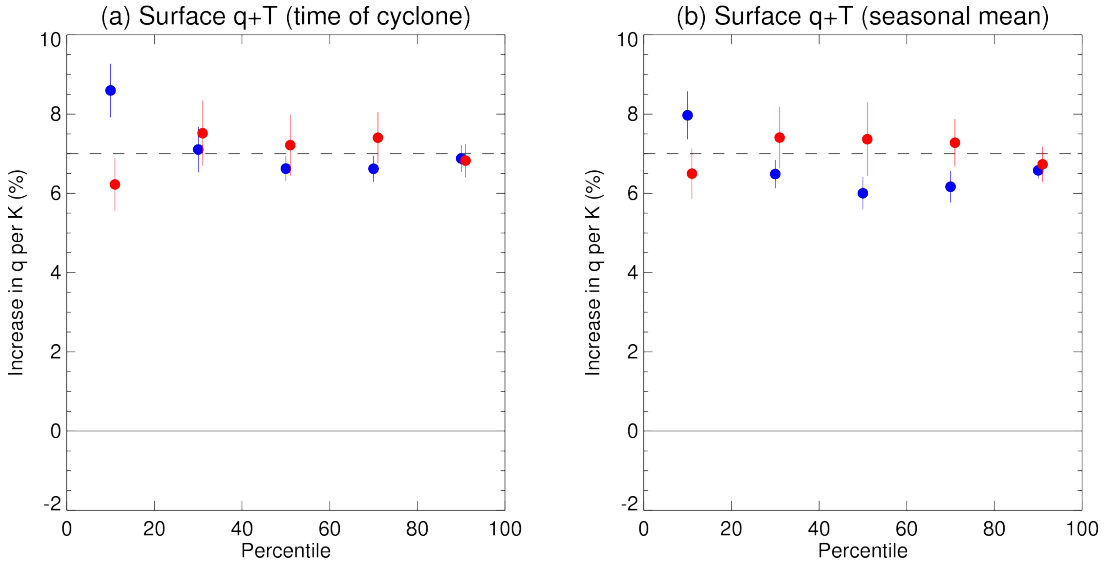


**Supplementary Figure 5**

Changes in near surface (~2m) specific humidity (% $K^{-1}$) scaled by near surface (~2m) air temperature using (a) the instantaneous and (b) seasonal mean near surface temperature and specific humidity at each location for DJF (blue) and JJA (red) with 95% uncertainty intervals. The x-axis percentiles are for maximum precipitation intensities such that this analysis includes the same cyclones as Supplementary Figure 3. Both humidity and temperature values are the mean within a 5° radial cap of the cyclone centre.

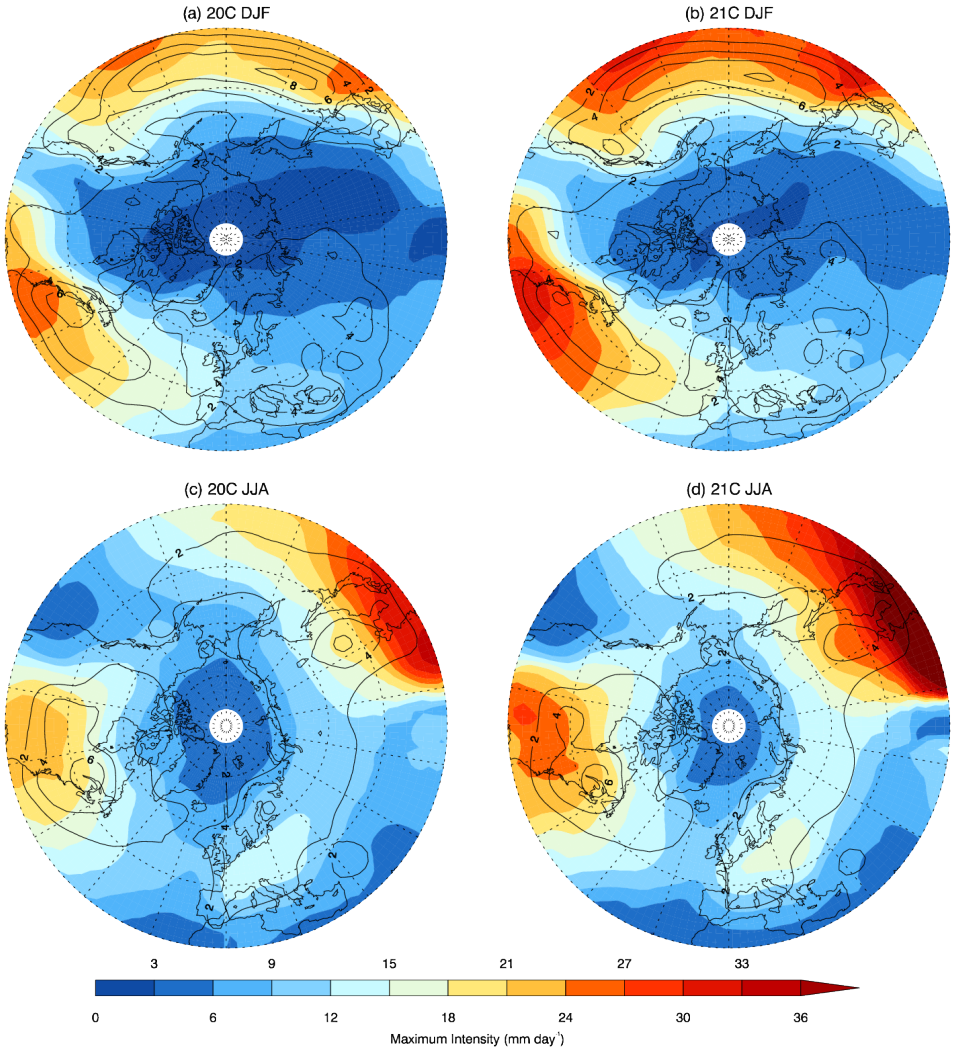


**Supplementary Figure 6**

Average maximum precipitation intensity of cyclones analysed in this study (coloured contours, mm day$^{-1}$) and cyclone density (line contours, intervals of 2 cyclones per month per unit area, which is a 5° spherical cap). Statistics are calculated using the point of maximum precipitation intensity from each cyclone track only. Precipitation intensity is calculated as the mean intensity within a 5° radial cap of the cyclone centre.

We further show in Supplementary Figure 5 that near surface specific humidity around cyclones scales at near to 7% K$^{-1}$ at all cyclone intensities when both the instantaneous (Figure 5(a)) and seasonal mean (Figure 5(b)) temperature and humidity changes are used. This again highlights the key role of low-level thermodynamic changes in governing the response of cyclones to a warming climate. These increases are slightly higher than global mean changes in surface specific humidity, but given the majority of these cyclones occur over the ocean, consistent with other findings*(45)*. The increases in surface specific humidity (~7% K$^{-1}$) are higher than those for precipitation, particularly in

the case of less intensely precipitating cyclones. More intensely precipitating cyclones typically have stronger updrafts and near surface convergence which is likely associated with their greater efficiency in converting increases in low level moisture into precipitation in those cyclones*(2)*.

## Section 5. Location of cyclones and the regions analysed in this study

Supplementary Figure 6 shows both the average maximum precipitation intensity of cyclones in this study and also the track density. The points shown in both cases are for the intensity and location of the point of maximum precipitation only, rather than points throughout each cyclone's lifecycle. In terms of storm location, the two primary winter storm track regions of the Atlantic and Pacific are clear (Supplementary Figure 6(a) and (b)), with the precipitation intensity being strongest on their southern flanks and in the storm track entrance regions. In summer, a more northerly but significantly weaker Pacific storm track is observed (Supplementary Figure 6(a) and (b)) and the highest density of occurrence is over North America. In the future, both the changes in feature distribution and intensity are, to first order, amplifications of the existing patterns, though with important changes at the regional scale, as has previously been documented*(14,17,19,21)*.

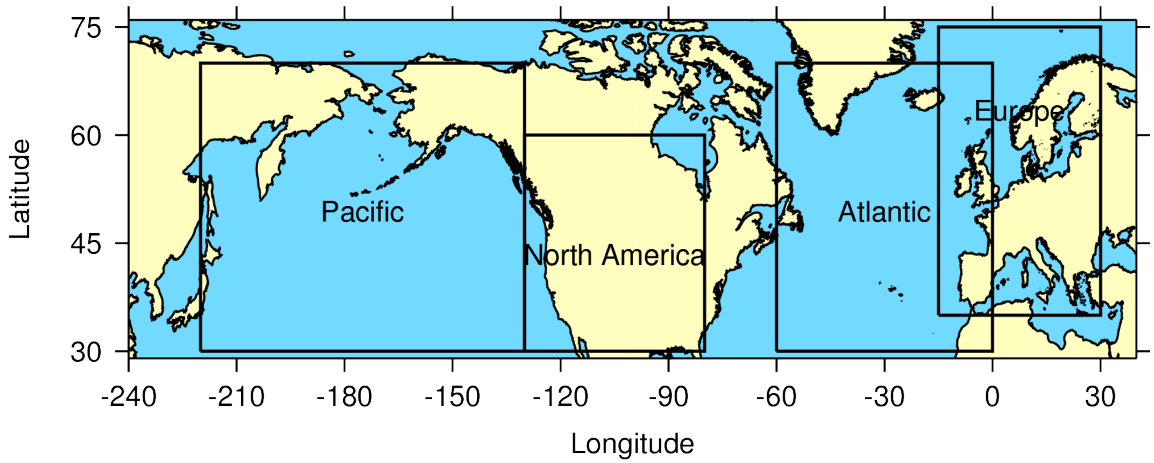


**Supplementary Figure 7**
Regions analyzed in the text. Storms are associated with a region if the maximum precipitation (based on the average precipitation within 5° of the cyclone centre) during the cyclone lifecycle occurs in that region.

In Figure 3, cyclones are analysed in four key regions of the Northern Hemisphere. Storms are subset by the location of their maximum precipitation intensity during their lifecycle. Those regions are shown in Supplementary Figure 7. The extent of each region is intended to include both the observed storm tracks and those in present day and future

model simulations, taking into account spatial biases in the models(*4,18,19*, see Supplementary Figure 6). We have tested the sensitivity of the conclusions to the latitudinal and longitudinal extent of these regions, finding the results remain qualitatively comparable irrespective of such changes (not shown).

## Section 6. Cyclone associated precipitation changes

Supplementary Figure 8 shows the fraction of precipitation which is cyclone associated (see Methods) in DJF and JJA, with the change in the fraction of total precipitation which is cyclone associated from the 20$^{th}$ to 21$^{st}$ centuries. Across the NH, the spatial distribution of cyclone associated precipitation replicates the key features seen in observations*(4)*. The winter storm tracks are clear in DJF, with 70-90% of total precipitation being cyclone associated. There are relatively small changes in the 21$^{st}$ century, with typical values of ±2%, and little consensus on the direction of change across the ensemble in the main storm track regions. In JJA, the fraction of total precipitation which is cyclone associated is lower, as the storm tracks are less active in the summer. Across North America and Europe, cyclones make a reduced contribution to total precipitation, though in the extreme these reductions are ~8%, such that the role of cyclone associated precipitation remains an important contributor to total precipitation.

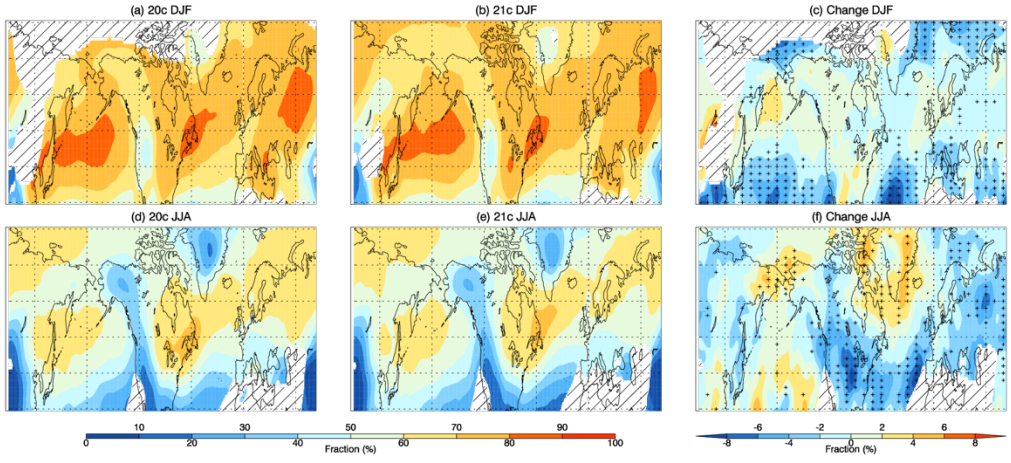


**Supplementary Figure 8**

Fraction of total precipitation which is cyclone associated in 20$^{th}$ (a,d) and 21$^{st}$ (b,e) centuries in DJF (a-c) and JJA (d-f), with the change in the fraction from 20$^{th}$ to 21$^{st}$ centuries (c,f). Regions where the total precipitation during the season is less than 0.5mm day$^{-1}$ are masked out. Stippling in c,f shows where <u>at least</u> 75% of the models agree on the direction of change.

Turning to changes in extreme cyclone associated precipitation, defined as the 99$^{th}$ percentile of 20$^{th}$ century cyclone associated precipitation at each gridpoint in the relevant season, Figure 4 shows substantial increases in cyclone associated precipitation in each season. In Supplementary Figure 9, the fraction of total precipitation associated with this extreme cyclone associated precipitation is also shown. Figure 4 gives an absolute change in this extreme cyclone associated precipitation, which may be considered particularly important for impacts such as flooding. In Supplementary Figure 9, the increases in the fraction of precipitation associated with these extreme events emphasises the wider impact these changes may have, as these cyclones deliver up to 20% of the total precipitation in parts of North America during DJF in the 21$^{st}$ century and 10-16% of precipitation across much of Europe. In JJA, values of 4-8% are typical in the 20$^{th}$ century which increase to 6-12% in the 21$^{st}$ century.

From a flood management perspective, return periods are frequently used to assess impacts. A detailed analysis of any change in flood risk would require considerable hydrological modeling and is outside the scope of this study, though high streamflow is related to heavy precipitation occurrence, particularly large-scale, organised events as analysed in this study *(12,46-48)*. Supplementary Figure 10 shows the frequency per season of extreme cyclone associated precipitation for both the 20$^{th}$ and 21$^{st}$ centuries and the change between the two. The patterns of change in Supplementary Figure 10(c,f) are unsurprisingly similar to Supplementary Figure 9 and show increases in extreme cyclone associated precipitation across North America and Europe during DJF, with events occurring up to 3 times as often (a 200% increase in frequency) in some regions. In JJA, there is lower consensus on the direction of change, with decreased event frequency in southern Europe and parts of the United States and up to a doubling of event frequency elsewhere across the two regions.

Together, these results show a clear shift in total precipitation towards large-scale, organised, heavily precipitating events, which may be at the expense of less frequent precipitation, with implications for water management, agriculture and flooding.

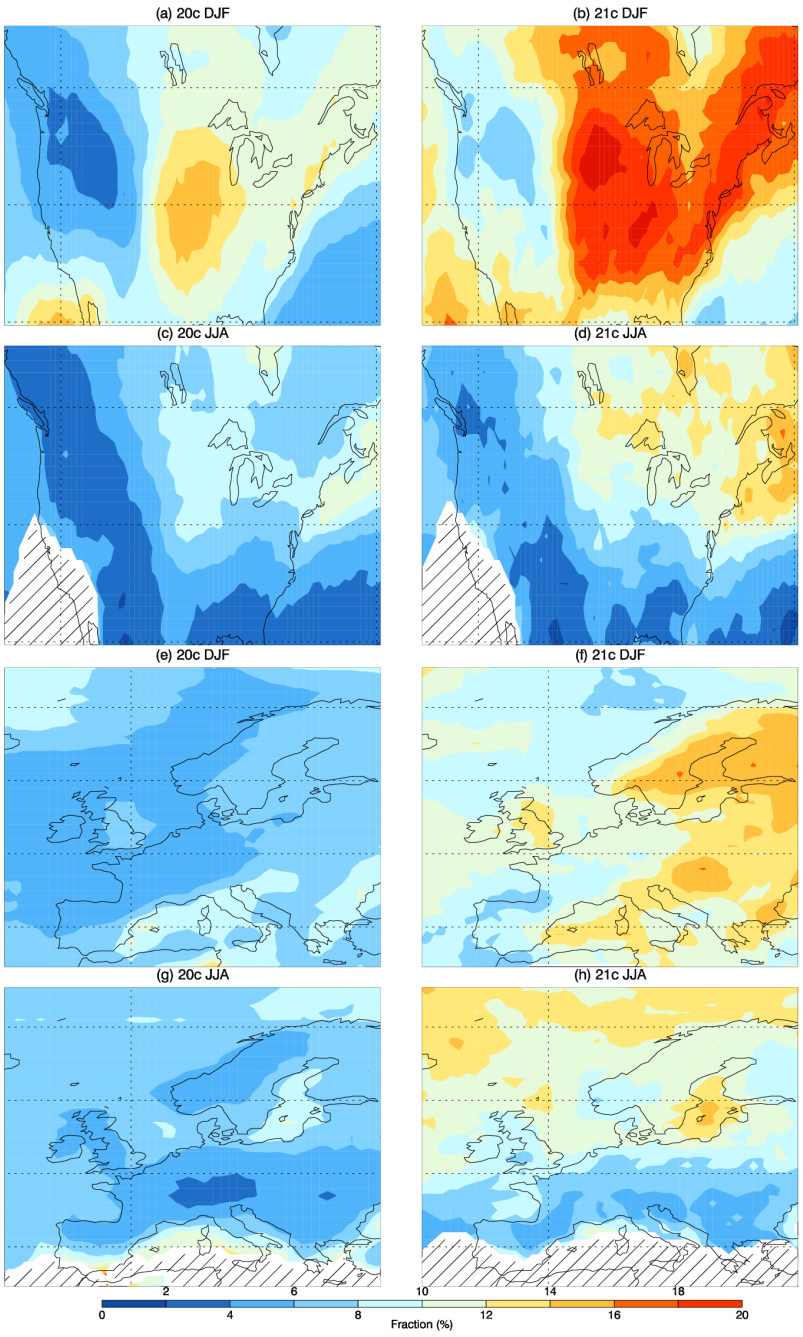


**Supplementary Figure 9**

Fraction of total precipitation which is extreme cyclone associated precipitation (>99$^{th}$ percentile of 20$^{th}$ century storm associated precipitation) for North America (a-d) and Europe (e-h) in 20$^{th}$ (a,c,e,g) and 21$^{st}$ (b,d,f,h) centuries for DJF (a,b,e,f) and JJA (c,d,g,h) Regions where the total precipitation during the season is less than 0.5mm day$^{-1}$ are masked out.

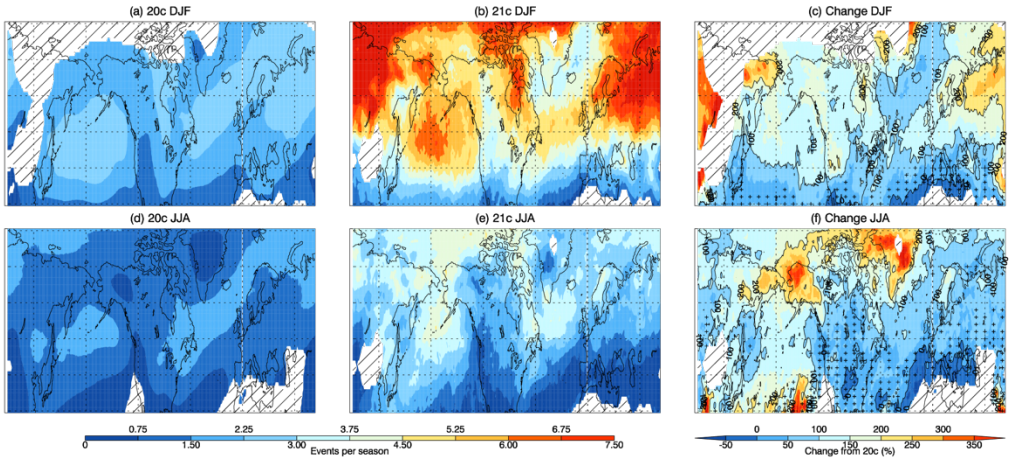


**Supplementary Figure 10**

Frequency of extreme cyclone associated precipitation events (>99$^{th}$ percentile of 20$^{th}$ century cyclone associated precipitation, per season) in 20$^{th}$ (a,d) and 21$^{st}$ (b,e) centuries in DJF (a-c) and JJA (d-f), with the change in the frequency from 20$^{th}$ to 21$^{st}$ centuries (c,f). Regions where the total precipitation during the season is less than 0.5mm day$^{-1}$ are masked out. Stippling in c,f shows where fewer than 75% of the models agree on the direction of change.

## Section 7. Model data used in this analysis

In this study, data was required at 6-hourly intervals on multiple model levels. This was not archived for all models participating in CMIP5 and we use the 16 models for which the relevant data was available at the time of the analysis (see Supplementary Table 1). A single ensemble member of each model was used for each of the present day and future analysis periods. Data is analysed for the periods DJF 1989/90-1998/99 and 2089/90-2098/99 and JJA 1990-1999 and 2090-2099.

| Model and Institution | | Atmospheric Resolution | |
|---|---|---|---|
| Model Name | Institution | Horizontal | Vertical |
| BCC-CSM1.1 | Beijing Climate Center, China | T42 (128x64) | 26 |
| BCC-CSM1.1(M) | Beijing Climate Center, China | T106 (320x160) | 26 |
| CCSM4 | Climate Community, USA | 288x190 | 26 |
| CMCC-CM | Centro Euro-Mediterraneo sui Cambiamenti Climatici, Italy | 480x240 | 31 |
| FGOALS-g2 | State Key Laboratory of Numerical Modelling for Atmospheric Sciences and Geophysical Fluid Dynamics, China | 128x60 | 26 |
| GFDL-CM3 | Geophysical Fluid Dynamics Laboratory, USA | 144x90 | 48 |
| GFDL-ESM2M | Geophysical Fluid Dynamics Laboratory, USA | 144x90 | 24 |
| GFDL-ESM2G | Geophysical Fluid Dynamics Laboratory, USA | 144x90 | 24 |
| INM-CM4 | Institute of Numerical Mathematics, Russia | 180x120 | 21 |
| IPSL-CM5A-LR | L'Institut Pierre-Simon Laplace, France | 96x96 | 39 |
| IPSL-CM5A-MR | L'Institut Pierre-Simon Laplace, France | 144x143 | 39 |
| MRI-CGCM3 | Meteorological Research Institute, Japan | TL159 (320x160) | 48 |
| MIROC5 | Model for Interdisciplinary Research on Climate, Japan | T85 (256x128) | 56 |
| MIROC-ESM | Model for Interdisciplinary Research on Climate, Japan | T42 (128x64) | 80 |
| MIROC-ESM-CHEM | Model for Interdisciplinary Research on Climate, Japan | T42 (128x64) | 80 |
| NorESM1-M | Norwegian Climate Centre, Norway | 144x96 | 26 |

**Supplementary Table 1**

CMIP5 models analysed in this study. The following information is shown in the table: model acronym, institution and atmospheric resolution. Dimensions of the Gaussian grids are shown in brackets for spectral models. It should be noted that surface specific humidity was not available for CMCC-CM so 15 models are included in Fig. S5. One ensemble member is used from each model.

**References in Supplementary Material (see Main Text for references 1-42)**

[43] Pinto J G , Neuhaus C P, Leckebusch G C, Reyers M and Kerschgens M 2010 Estimation of wind storm impacts over Western Germany under future climate conditions using a statistical–dynamical downscaling approach. *Tellus A*, *62*(2), 188-201.
[44] Dawkins L C, Stephenson D B, Lockwood J F and Maisey P E 2016 The 21st century decline in damaging European windstorms. *Natural Hazards and Earth System Sciences*, *16*(8), 1999.
[45] O'Gorman P A and Muller C J 2010 How closely do changes in surface and column water vapor follow Clausius–Clapeyron scaling in climate change simulations? *Environmental Research Letters*, *5*(2), 025207.
[46] Easterling D *et al*. 2000 Climate extremes: observations, modeling, and impacts. *Science* 289.5487: 2068-2074.
[47] Groisman P Y, Knight R W and Karl T R 2001 Heavy precipitation and high streamflow in the contiguous United States: Trends in the twentieth century. *Bulletin of the American Meteorological Society* 82(2) 219-246.
[48] Pall P *et al* 2011 Anthropogenic greenhouse gas contribution to flood risk in England and Wales in autumn 2000 *Nature* 470(7334) 382-385.